Journal of Materials Chemistry A

ROYAL SOCIETY OF CHEMISTRY

PAPER

View Article Online
View Journal

Cite this: DOI: 10.1039/d6ta00758a

Optimal electrolyte pH for efficient quinone-based aqueous redox flow battery and solar cell integration

Joao Otavio Mendes, [a] Rasmus Svejstrup Nielsen, [a] Tobias Høyrup Hemmingsen, [a] Thomas K. Rønne-Nielsen, [b] Susanne Mossin, [b] Ole Hansen [c] and Peter Christian Kjærgaard Vesborg *[a]

Quinone-based redox flow batteries (RFBs) have emerged as promising sustainable alternatives to conventional vanadium systems, offering lower costs, high abundance and compatibility with large-scale aqueous energy storage systems. Their tuneable redox potential with pH can also enable direct integration with photovoltaic (PV) devices for solar charging. However, the design of efficient quinone electrolytes requires a detailed understanding of pH-dependent proton-coupled electron transfer, which drives fast or sluggish reaction kinetics. Here, we apply a pH buffering method to a 2,7-AQDS anolyte to tune the cell voltage, enabling efficient operation of a proof-of-concept solar redox flow battery (SRFB) with maximised solar-to-output electricity efficiency (SOEE). We also investigate how pH affects the charging reaction pathway and the voltage efficiency (VE), establishing that a buffered 2,7-AQDS anolyte achieves optimal performance at pH 8–10. These findings provide key insights into device integration and the pH dependence of VE in this quinone electrolyte. Importantly, this work establishes practical guidelines for pH optimisation in the design of next-generation quinone-based aqueous RFB and SRFB technologies.

Received 26th January 2026
Accepted 20th April 2026

DOI: 10.1039/d6ta00758a

rsc.li/materials-a

Introduction

Research on aqueous redox flow batteries (RFBs) has increasingly focused on organic redox-active molecules as alternatives to conventional vanadium-based chemistries.[1–4] Among other promising candidates – including TEMPO derivatives, viologens, and azo compounds – quinones have been extensively investigated for RFB applications due to their highly reversible redox reactions and favourable kinetics.[5] Sulfonated anthraquinones, in particular, offer high water solubility and yield stable aromatic reduction products.[6] Anthraquinone-based aqueous anolytes can deliver capacities exceeding 40 Ah L^{-1} through a one-step two-electron redox process.[6,7] These properties make quinones a highly attractive class of molecules for utility-scale aqueous RFBs.

Quinone derivatives and related molecules (catechol and anthraquinone) also offer a vast array of electrochemical properties for application in novel cell architectures including hybrid flow batteries, redox-targeting systems and integrated solar redox flow batteries (SRFBs).[8–12] Nevertheless, in aqueous electrolytes the redox reactions of quinones are coupled to protonation–deprotonation equilibria of carbonyl groups, with the exact reaction pathway determined by the electrolyte pH.[13] This characteristic coupled electron–proton transfer makes both the standard redox potential and kinetics of quinones strongly pH dependent and directly impacts device performance.[14–16]

The pH-dependent redox behaviour of quinones enables useful applications. Khataee *et al.*[17] employed a differential pH method to significantly increase the RFB cell voltage (E_{cell}). In an RFB containing the pH-dependent redox anolyte 2,7-anthraquinone disulfonic acid (2,7-AQDS) and pH-independent redox bromide as the catholyte, E_{cell} is significantly higher with 2,7-AQDS at pH 8 ($E_{cell} = 1.3$ V) compared to the same RFB with 2,7-AQDS at pH 2 ($E_{cell} = 0.86$ V). The Nernstian shift in the redox potential of quinones with pH has also been applied to voltammetric pH sensing.[18]

Fine-tuning E_{cell} can be achieved using pH buffers,[19] and it is extremely useful for fabricating efficient SRFBs.[20] The concept of an SRFB has attracted attention as an approach to seamless integration of energy storage systems and photoelectrodes. SRFBs were first demonstrated with the integration of simple semiconductors,[21,22] and more recently the use of photovoltaic (PV) cells allowed for more efficient systems.[23–26] However, integration of a highly efficient PV cell with a high performing RFB does not ensure high SRFB performance. McCulloch *et al.*[20]

[a]SurfCat, DTU Physics, Technical University of Denmark, Kongens Lyngby 2800, Denmark. E-mail: peter.vesborg@fysik.dtu.dk
[b]DTU Chemistry, Technical University of Denmark, Kongens Lyngby 2800, Denmark
[c]National Centre for Nano Fabrication and Characterisation (DTU Nanolab), Technical University of Denmark, 2800 Kongens Lyngby, Denmark

demonstrated that tuning the pH of 2,7-AQDS anolyte can be used to adjust the RFB E_{cell} and maximise the power of a 2,7-AQDS/Iodine SRFB powered by a dye-sensitised photoelectrode. More recently, solar-to-output electricity efficiency (SOEE = $E_{electrical,discharge}/E_{illumination}$) has been introduced as a metric to measure the round trip efficiency of SRFB systems.[23,24,27] As a general principle, SOEE reaches a maximum when the RFB E_{cell} matches the voltage at the maximum power point (V_{mpp}) of the solar cell.[28] Thus, the McCulloch method can be used to adjust E_{cell} and maximise the voltage matching in SRFBs.

The pH-tuning method introduced by McCulloch presents a straightforward and practical strategy to fine-tune the RFB E_{cell} for integration of RFBs with a desired PV device. However, pH changes directly influence the performance of quinone-based batteries. Specifically, the reaction pathways prevailing at a given pH drive the kinetic behaviour of the electrolyte (fast or sluggish), thereby impacting the battery voltage efficiency (VE). Therefore, a comprehensive investigation of how electrolyte pH impacts VE in quinone-based electrolytes is required, not only to realise the maximum achievable SOEE in SRFBs, but also to elucidate the optimal electrolyte pH for maximum VE in RFBs.

In this work, we optimise the operating voltage of a proof-of-concept aqueous SRFB, integrating it with a selenium (Se) PV cell. Similarly to the McCulloch method, the RFB E_{cell} is tuned by buffering 2,7-AQDS anolyte at precise pH values, maximising SOEE. Furthermore, we conduct a comprehensive pH optimisation study based on the anolyte charging reaction pathway. Using cyclic voltammetry (CV), CV simulations, and a three-electrode battery cell, we quantify the VE of an RFB as a function of anolyte pH. This approach allows us to identify the optimal operating pH for maximum VE of an electrochemical cell using 2,7-AQDS as the anolyte. Importantly, our pH optimisation approach may be applicable to other quinone-based electrolytes, provided that the charging reaction pathways are known.

Experimental

Materials

Sodium 9,10-dioxo-9,10-dihydroanthracene-2,7-disulfonate (≥80%) was purchased from BLD Pharm. Sodium hexacyanoferrate(II) decahydrate (≥98.0%), potassium hexacyanoferrate (III) (≥99.0%), sodium chloride (≥99%), 1,2-propanediol (99%), ammonium chloride (≥99.5%), phosphoric acid (85%), tris·HCl (tris(hydroxymethyl)aminomethane hydrochloride, ≥99%), acetic acid (≥99.7%) and sodium hydroxide (≥98%) were obtained from Sigma Aldrich. All reagents and solvents were used as received without further purification. The cation exchange membrane (Nafion-117) was treated with ~80 °C 3% H_2O_2, Milli-Q water, 0.5 M H_2SO_4 and 1 M NaOH successively for ~2 h per step. Graphite soft felt (Sigratherm GFD 4.65 EA, SGL Carbon) was activated by thermal treatment for at least 10 h at 400 °C in a muffle oven without atmospheric control. Graphite sheet (RS PRO 0.16 mm) from RS. Alumina polishing compound (50 nm). Micro reference electrode (Ag/AgCl). The FTO-coated soda-lime glass (SLG) was bought from Sigma-Aldrich (7 Ω sq^{-1}). $Zn_{0.85}Mg_{0.15}O$ (99.95 + %), MoO_3 (99.9%), and Au (99.99%) sputtering targets were acquired from AJA International, while Te (99.9999% metals basis) and Se (99.999 + % metals basis) pellets were sourced from Alfa Aesar.

Instrumentation

Throughout this work, pH was measured with an Orion Star A111 pH meter equipped with a calibrated Orion single junction pH/ATC triode from Thermo Scientific. The electrolyte was circulated *via* two peristaltic pumps LabS3 from Shenchen. Electrochemical and battery measurements were conducted with potentiostat/galvanostat ref. 620 from Gamry. During solar charge, the current was measured using a homemade current meter consisting of a INA219 chip installed on an Arduino Nano interface. The simulated sunlight was produced using a 66 921 arc lamp housing equipped with 1000 W Xe arc lamp, water infrared filter (6123NS) and light guide (fibre optic bundle, high grade fused silica, 260–2200 nm), all from Newport. To assess the Se solar cell stability during battery charge, the power conversion efficiency (PCE), V_{mpp} and J_{mpp} were extracted from *JV* curves collected over time during constant light exposure using a Keithley 2561A source meter and 1 sun AM1.5 G illumination from solar simulator equipped with a 1600 W Xe arc lamp (Newport).

Preparation of buffer and electrolytes

The anolyte solutions contained an aqueous mixture of ~10 mM 2,7-AQDS as the only redox-active molecule, a universal buffer (0.1 M H_3PO_4, 0.1 M CH_3COOH, 0.1 M tris·HCl and 0.1 M NH_4Cl), supporting electrolyte (1 M NaCl), an additive for solubility enhancement (10% v/v propylene glycol), and NaOH (for pH adjustment). The initial buffer solution was prepared using the protonated forms of species (acids). Buffer pairs were chosen to provide approximately evenly spaced pK_a values,[29,30] *i.e.* phosphoric acid (pK_{a1} = 2.1, pK_{a2} = 7.2, pK_{a3} = 12.0), acetic acid (pK_a = 4.74), tris·HCl (pK_a = 8.1) and ammonium chloride (pK_a = 9.24) at 0.1 M final concentration of each acid. Sodium chloride was then added to the buffer to a final concentration of 1 M, followed by the addition of propylene glycol to 10% v/v and 2,7-AQDS to ~10 mM. These mixtures (pH ≈ 1.5) were then sonicated for 10 min at ~40 °C in an open vial to release CO_2.[17,31] Finally, the pH was raised with a 5 M or 10 M NaOH solution as needed. The catholyte solutions were prepared simply by mixing redox-active species (30 mM $Fe[(CN)_6]^{4-}$ and 10 mM $Fe[(CN)_6]^{3-}$) and supporting electrolyte (1 M NaCl) without any buffer or pH adjustment. The pH on the catholyte side was tested with a pH paper before and after cycling and it was verified that it remained approximately constant at ~4.

Electrochemical and battery measurements

CV measurements were conducted in a three-electrode cell. The working electrode consisted of a glassy carbon disk with 5 mm diameter that was polished with alumina compound, rinsed and sonicated in Milli-Q water immediately before use. A Pt wire was used as counter electrode. The electrolytes consisted of

buffered solutions of ~10 mM 2,7-AQDS (or hexacyanoferrate solution) in 1 M NaCl. The sweep speed was typically 100 mV s^{-1} and the voltage interval was adjusted according to the species redox potential and solution pH. Galvanostatic cycling was conducted in an airtight two- or three-electrode flow cell containing 10 mL of ~10 mM of 2,7-AQDS anolyte and 10 mL of sodium hexacyanoferrate solution (30 mM $Fe[(CN)_6]^{4-}$ and 10 mM $Fe[(CN)_6]^{3-}$) as catholyte. Both the anolyte and catholyte were pumped at approximately 70 mL min^{-1} through the cell. For the three-electrode tests, the RE was inserted in the anolyte side of the cell. The system was purged with Ar for at least 15 min before the start of each measurement. For characterisation of the semi-integrated system, the selenium solar cell was mounted in an external holder, connected to the battery, and the light guide was attached to the holder. During solar charge the current was measured in the current meter, while the battery voltage was monitored directly on the potentiostat. When the limiting voltage was achieved, a relay was activated to disconnect the solar cell from the system and close the solar simulator shutter. After that, the discharge program was initiated by the potentiostat.

Fabrication of Se solar cells

The fabrication of selenium solar cells is well established in our research group.[32–34] Here, they were made in the SLG/FTO/ZnMgO/Te/Se/MoO_x/Au superstrate configuration. A ~65 nm ZnMgO thin film was deposited *via* reactive RF sputtering from a ceramic target (Ar/O_2 = 60/0.6 sccm, 5 mtorr) on a clean FTO-coated glass substrates (sequential ultrasonic bath with Milli-Q water, acetone and isopropanol followed by drying under N_2 flow). The glass/FTO/ZnMgO were transferred to a custom-built thermal evaporator for deposition of a 1 nm Te adhesion layer (base pressure ~10^{-8} mbar, rate 0.25 Å s^{-1}). Without breaking vacuum, a ~300 nm of selenium is thermally evaporated on top of glass/FTO/ZnMgO/Te (rate 4 Å s^{-1}). The glass/FTO/ZnMgO/Te/Se are then placed in a pre-heated home-built aluminium oven where the as-deposited Se crystallises (190 °C in air for 4 min). A hole transport layer consisting of MoO_x is deposited on the glass/FTO/ZnMgO/Te/Se samples using RF sputtering of ceramic MoO_3 (Ar/O_2 = 60/0.6 sccm). The devices are completed by DC sputtering a ~50 nm Au back contact to achieve the final SLG/FTO/ZnMgO/Te/Se/MoO_x/Au configuration. The final active device area is 0.8 cm^2.

Fabrication of redox flow battery and semi-integrated system

Battery tests were conducted in a flow cell. In summary, the cell consists of two PEEK flow fields (half cells) with 10 × 10 mm aperture. The cation exchange membrane is sandwiched between two 10 × 10 × 4.6 mm carbon felt electrodes that are fitted in the half cells and are in contact with graphite sheet current collectors. The graphite sheet is electrically connected to copper tape contacts that are isolated from the electrolyte. The solar cell is integrated into the system externally and does not contact the electrolyte.

Simulation of cyclic voltammetry curves

CV curves were simulated at various pH values using electrochemistry simulation software MECSim script and following the method previously described in the literature.[35,36] In short, pH changes can be simulated by assuming a 1st order reaction with proton concentration and setting $k_f = k_{f,max}[H^+]$ for the chemical steps, while electron transfer rates (k^0) are used on the electrochemical steps. Simulation parameters were taken from the literature[36,37] and are available in Table S2. Additionally, temperature was set to 25 °C (298.15 K), electrode diameter to 5 mm, and scan speed was varied as needed. The apparent kinetic constant (k_{app}) was extracted from the simulated CV curves using the equations for a totally irreversible system[38,39] and the Nicholson method (quasireversible system).[40,41]

Results and discussion

Solar and electrochemical cell integration

The integration of the 2,7-AQDS/ferrocyanide RFB with the solar cell follows the voltage matching principles introduced by Li *et al.*[27] In this method, simulated Nernstian RFB charging curves are matched with the experimental solar cell current density *vs.* voltage (*JV*) curves. Maximum SOEE is obtained when E_{cell} is close to the voltage at the maximum power point of the solar cell ($E_{cell} \approx V_{mpp}$).[24] Fig. 1a shows a scheme of the system used in this work. Here, a Se solar cell (Fig. S1a) is integrated outside the battery. Except for external contact resistances, the absence of a liquid junction between the solar and electrochemical cells is not expected to affect the voltage matching. The photovoltage arises at the internal solid-state junctions of the solar cell and the system behaves as if it were monolithically integrated in terms of SOEE. The Se solar cell was chosen for this integration due to our group's previous expertise and due to the wide bandgap of selenium (1.8–2 eV) that allows for a high open circuit voltage ($V_{oc} \approx 1$ V) and can potentially produce a high V_{mpp}.[34] Additionally, the bandgap of selenium is close to ideal for tandem integration with silicon solar cells.[33,42] The 2,7-AQDS was chosen as the active species at the anolyte side due to its high solubility in water and adjustable redox potential.[43] In aqueous solution, the redox potential of 2,7-AQDS varies with pH according to the Nernst equation over a certain pH range.[19] As such, the 2,7-AQDS/ferrocyanide E_{cell} may be tuned simply by varying the anolyte pH,[20] as illustrated by the CVs in Fig. 1b.

Initially, we evaluate the solar cell and RFB separately. We first obtain the *JV* curve of a typical Se solar cell (PCE = 4.9%, V_{OC} = 0.78 V and J_{SC} = 12.7 mA cm^{-2}), as shown in Fig. 1c, and calculate the SOEE, as described in the SI (calculated SOEE and voltage matching).[23,27] The SOEE was numerically computed for E_{cell} varying from 0.3 to 0.7 V. For this Se cell, the maximum round trip efficiency was obtained at E_{cell} = 0.52 V, Fig. 1d. Then, we determined how E_{cell} varies as a function of the anolyte pH by cycling the battery with an anolyte solution buffered at a desired pH. Anolyte pH was buffered with a universal buffer solution (0.1 M H_3PO_4, 0.1 M CH_3COOH, 0.1 M Tris·HCl and 0.1 M NH_4Cl) and adjusted with NaOH. To isolate the effects of pH, this buffer was carefully designed so that it is chemically

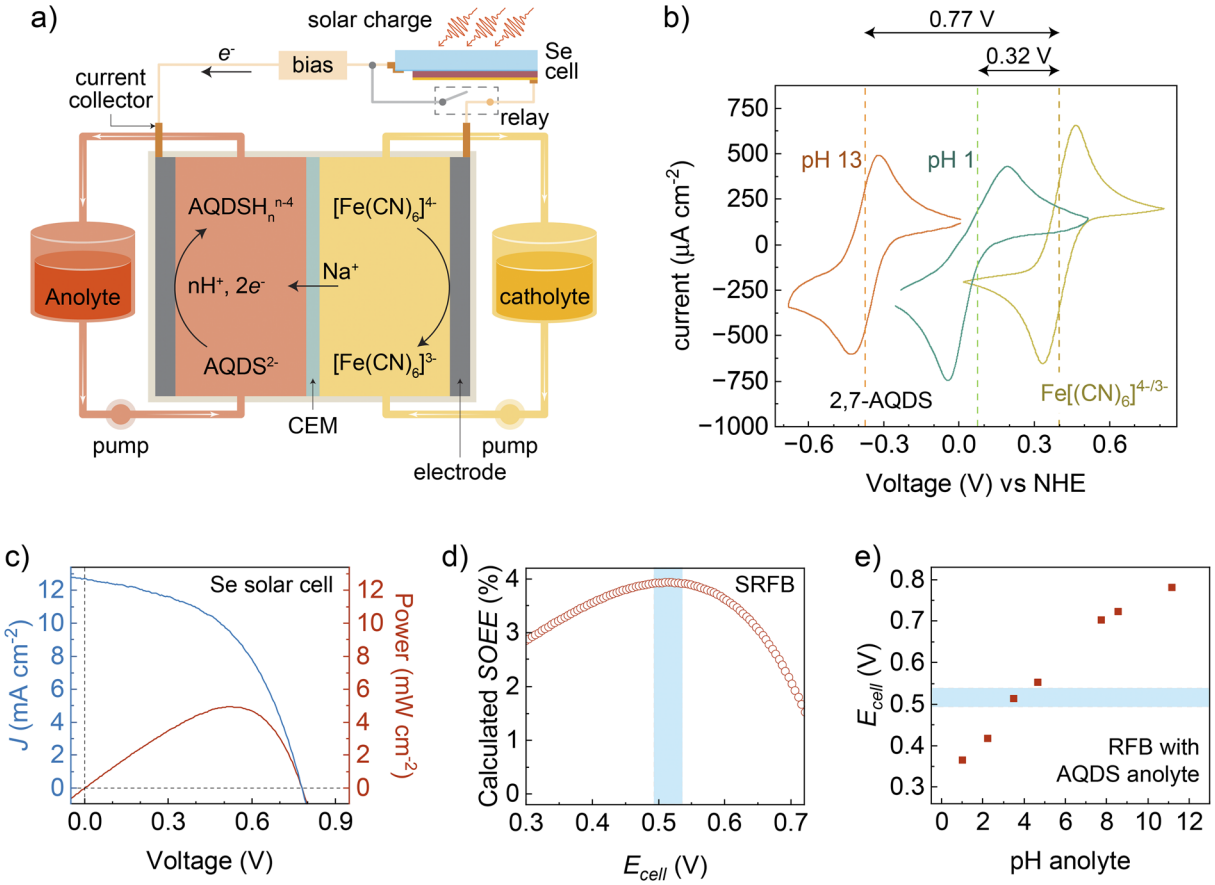

Fig. 1 (a) Schematic representation of solar charge in 2,7-AQDS/ferrocyanide SRFB, (b) CVs of AQDS anolyte buffered at pH 1 and 13 and of ferrocyanide catholyte, (c) *JV* and power curves of Se solar cell at AM1.5 G, (d) calculated SOEE for the Se solar cell integrated to a battery with energy efficiency of EE = 85% and (e) measured cell voltage at 50% SOC (E_{cell}) and 5.36 mA cm^{-2} of 2,7-AQDS/ferrocyanide flow battery cell with anolyte buffered at pH 1–12.

and electrochemically inert under our experimental conditions. Furthermore, the same electrolyte composition was used for all battery measurements, only changing the amount of NaOH added to adjust the pH, as detailed in the Experimental Section and SI (Fig. S2). The E_{cell} shown in Fig. 1e was taken as the potential at 50% state of charge (SOC) in the first charging cycle at the slowest measured rate (5.36 mA cm^{-2}). An E_{cell} in the targeted range (~0.5 V) is obtained when 2,7-AQDS is buffered at pH ≈ 4. The full charging cycles and battery parameters for each investigated pH can be found in the SI (Fig. S3 and S4). In summary, the SOEE should be maximum when the Se solar cell is integrated with our 2,7-AQDS(pH ≈ 4)/ferrocyanide electrochemical cell.

After assessing the solar and electrochemical cell separately, we then study the integrated system. Our SRFB was evaluated with the 2,7-AQDS anolyte buffered within a relevant pH range (pH 1.0, 2.3, 4.7 and 7.0). The experimental SOEE was computed as explained in the SI (Experimental SOEE). As expected, higher SOEE values were obtained when the anolyte was buffered at intermediate pH values, Fig. 2a. The charging curves for the first cycle at each pH are also shown in Fig. 2b. For the anolyte buffered at pH 1.3, E_{cell} is very low (0.33 V), resulting in excess voltage produced by the solar cell that does not contribute to charging the battery and is wasted. At intermediate anolyte pH values, 2.3 and 4.7, the E_{cell} has a better voltage match (0.42 V and 0.54 V, respectively) and the system operates at higher SOEE values, 2.99% and 2.97%, respectively. When the anolyte is buffered at pH 7.0, E_{cell} is too high (0.66 V) and the voltage output from the solar cell is insufficient to fully charge the battery. This is better visualised by plotting the instant solar-to-output energy efficiency ($SOEE_{ins}$) that provides a snapshot of the SOEE at a specific SOC, as shown in Fig. 2c. With the anolyte at pH 7.0, the $SOEE_{ins}$ drops close to zero at approximately 65% SOC, and the battery cannot charge beyond this point. These results demonstrate that pH buffering of a quinone anolyte serves as an effective tool for achieving adequate voltage matching in SRFBs to improve the SOEE.

The cycling stability of our SRFB was tested over three charging cycles. Some degradation of the Se solar cell efficiency was observed during the charging period, as the solar cell is constantly exposed to light. This is shown in Fig. 2a. The red dotted line represents the SOEE calculated from the Se cell *JV* curve before any constant light exposure (pristine Se cell), while the blue dotted line represents the SOEE calculated from the *JV* curve obtained right after a full charge period. These efficiency losses can be attributed to a decrease in V_{mpp} when the Se cell is

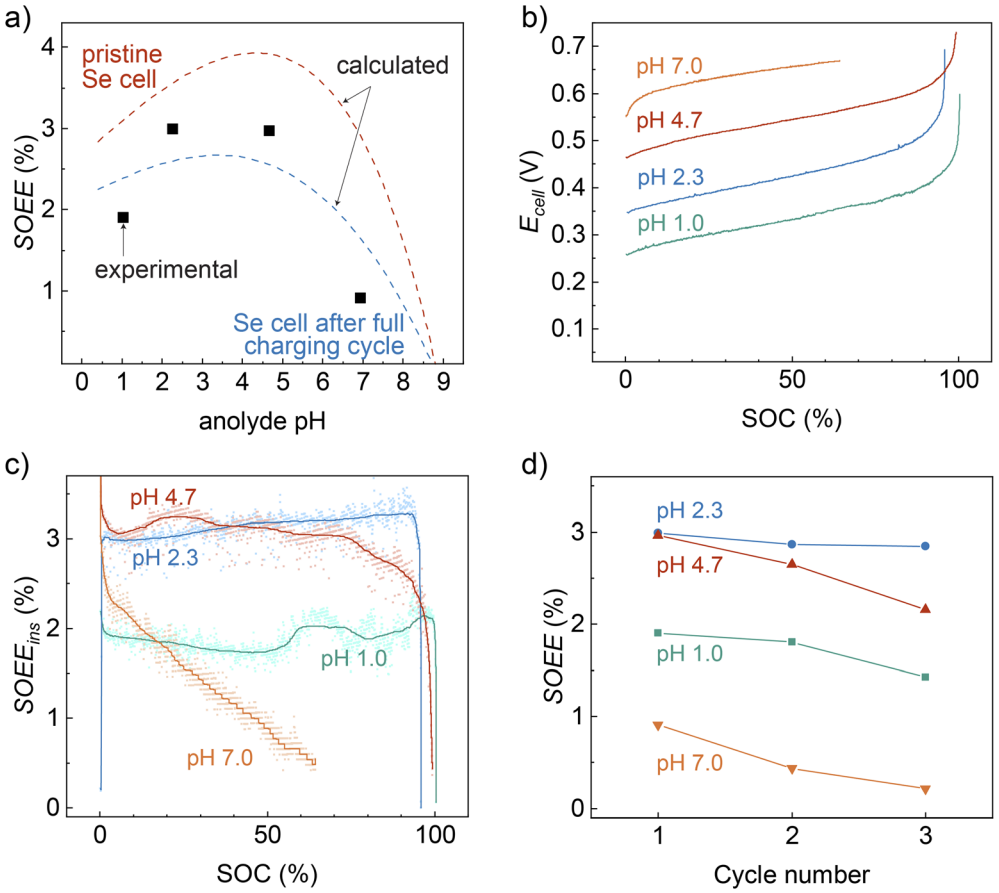

Fig. 2 SRFB powered by Se solar cell (a) calculated (dotted lines) and experimental (squares) SOEE. Experimental (b) charging curves, (c) $SOEE_{ins}$ and (d) system stability for a device with 2,7-AQDS anolyte buffered at different pH values. Dotted lines in panel '*a*' represent the calculated SOEE from *JV* curves obtained from Se cell before (pristine) and after a full charge cycle, with a battery energy efficiency of EE = 85%.

under constant light exposure (Fig. S1b), which directly impacts the voltage matching between the solar and electrochemical cells and results in a lower SOEE. Although the Se cell partially recovers during the discharge period when it is kept in the dark (Fig. S1b–d), an overall drop in SOEE is still observed in successive charge–discharge cycles, Fig. 2d (extra cycles are shown in Fig. S1e).

Battery voltage efficiency and reaction pathway

Clearly, buffering the anolyte pH can be used to tune the RFB E_{cell} and improve SRFB voltage matching.[20] However, the consequences of buffering the 2,7-AQDS at different pH values still need to be fully understood. To test how pH affects the RFB VE and CE, the anolyte pH was again adjusted to the desired value using our universal buffer and NaOH solution, similar to the SRFB tests. Battery parameters were calculated using the equations available in the SI (Table S1). Fig. 3a shows that CE decreases with increasing anolyte pH. This may be a consequence of side reactions involving the anolyte becoming more favourable at more negative potentials and may be addressed by purging residual oxygen or cycling at a more conservative voltage range. Meanwhile, VE tends to increase with increasing anolyte pH, resulting in a slight overall increase in energy efficiency (EE) at higher pH. As E_{cell} increases with anolyte pH, an increase in VE is expected, because VE accounts for the fraction of voltage lost during the round trip. However, as shown in Fig. 3b, the VE does not follow the expected trend for a constant voltage drop. Instead, the experimental VE exhibits complex behaviour: starting from low pH, the VE initially decreases to a minimum at pH 2–4, then increases to a maximum at pH 8–10 and decreases again at higher pH. Fig. 3c highlights the difference between expected and experimental VE (VE deviation). To quantify the voltage losses, an average voltage drop during the round trip (E_{drop}) can be defined (Table S1). For the investigated pH values, E_{drop} is maximum at pH 3.5 and minimum at pH 8.6 (Fig. 3d).

To gain a deeper insight into the impact of the anolyte pH on the battery VE, we first need to consider the charging reaction pathway of 2,7-AQDS in buffered electrolyte, as represented in the diagram of squares shown in Fig. 4.[36] In these diagrams, the rows represent electrochemical reactions (E), while the columns represent chemical reactions (C) that consist of a proton transfer. The pK_a and E_n values in Fig. 4a, taken from the literature, are provided in the SI (Table S2).[36] Missing values for 2,7-AQDS are assumed to be close to those determined for 2,9-AQDS.[37] The pathway for charge transfer at a given pH is directly

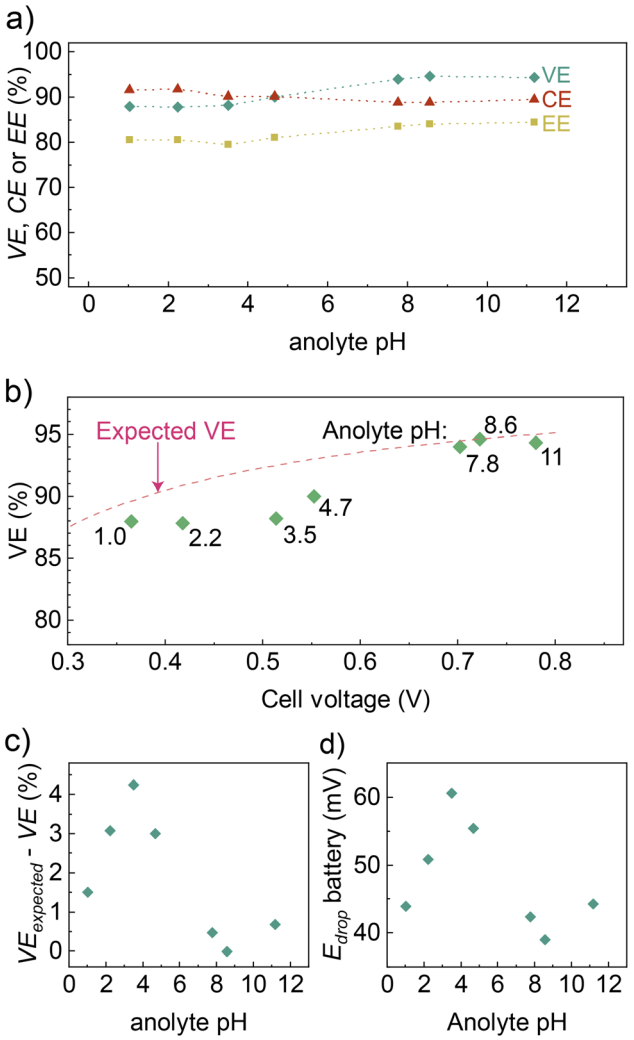

Fig. 3 Redox flow battery efficiency with buffered 2,7-AQDS anolyte (a) VE, CE and EE (b) expected and experimental VE at various pH values, (c) deviation from expected VE and (d) average cell voltage drop on the round trip (E_{drop}). Expected VE was calculated for a constant E_{drop} = 40 mV.

related to the species pK_{an} and the redox potential of the electrochemical step (E_n). Therefore, considering the pK_{an} and E_n values, the dominant reaction pathway for charging (reducing) the completely discharged (oxidised) 2,7-AQDS molecule can be inferred. At low pH ($0 \leq pH \leq 3$), the molecule is protonated before reduction takes place and a CECE reaction pathway dominates (Fig. 4b, panel 1). At intermediate pH ($4 \leq pH \leq 7$), reduction takes place before protonation and an ECEC reaction pathway is favoured (Fig. 4b, panel 2). At higher pH ($8 \leq pH \leq 10$), most molecules are completely reduced before protonation and an EECC reaction pathway dominates (Fig. 4b, panel 3). This shifts to a simpler EE reaction pathway (Fig. 4b, panel 4) at even higher pH (>10.6) when the majority of molecules are completely deprotonated at equilibrium, as indicated by the fraction composition diagram in Fig. S5.[36]

Further insight on the optimal operational pH for the 2,7-AQDS anolyte can be attained through CV experiments. The CVs

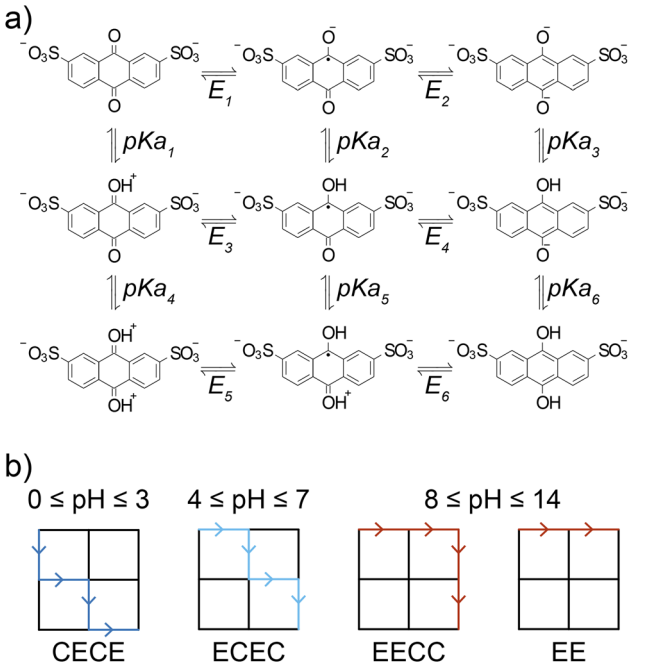

Fig. 4 Diagram of squares showing (a) 2,7-AQDS species in each redox step, and (b) probable predominant reaction pathway during charge of the 2,7-AQDS at the given pH range. Here, rows indicate electrochemical reactions (E), and columns chemical (protonation) reactions (C).

shown in Fig. 5a were obtained from 2,7-AQDS solutions buffered using our universal buffer solution in a regular three-electrode cell with a polished glassy carbon disc as the working electrode, as described in the Experimental Section. Fig. 5b shows how the anodic and cathodic peak potentials (E_p) vary as a function of pH. The experimental average peak potential ($E_{1/2}$) was fitted by eqn (S1) and plotted as a dashed line in Fig. 5b.[7] The buffered quinone solutions present a very distinct behaviour when compared to unbuffered solutions (Fig. S6). From pH $\approx$ 1 to 7 the value of $E_{1/2}$ decreases fast following the Nernst equation compatible with the transfer of $2e^-/2H^+$ ($n \approx 2$, eqn (S2)), *i.e.* CECE or ECEC reaction pathway dominates. It shifts towards a slower variation in $E_{1/2}$ with prevalence of EECC until *a* point (pH > 10.6) where $E_{1/2}$ nearly plateaus, indicating that electron transfer is not accompanied by proton transfer, *i.e.* the dominant EECC pathway shifts to the essentially electrochemical EE reaction pathway.

Changes in the charge transfer pathway (from CECE to ECEC to EECC and finally EE) are reflected in the shape of the CV curves, as well as in the pH-dependent trends of ΔE_p and i_p. Most notably, the charge transfer kinetics change from irreversible (large ΔE_p) at lower pH to reversible (small ΔE_p) at higher pH, Fig. 5c. At low pH, when the sluggish CECE reaction pathway prevails, ΔE_p increases with pH, reaching a maximum at pH 2–4 (pH 2.4 within measured points). When the reaction pathway shifts to predominantly ECEC, ΔE_p starts to decrease, reaching a minimum at pH 8–10 (pH 9.3 within measured points) when the main reaction pathway is EECC. The minimum ΔE_p at pH 8–10 corresponds to the lowest

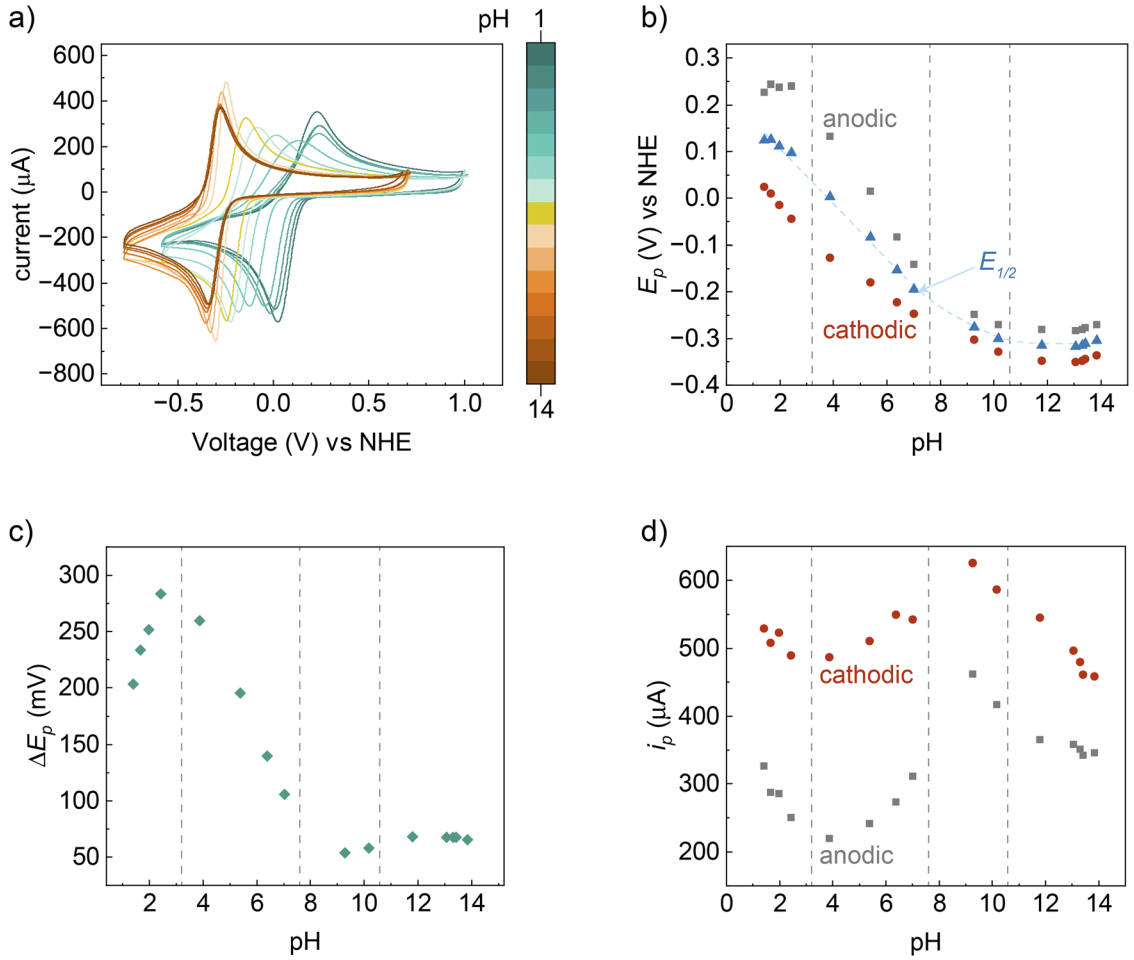

Fig. 5 Measured cyclic voltammetry (CV) data for buffered 2,7-AQDS solutions with pH varying from 1 to 14 showing the (a) CV curves, (b) peak positions, (c) peak separation and (d) absolute peak currents. Dashed lines indicate relevant pK_a values (pK_{a1} = 3.2, pK_{a3} = 7.6 and pK_{a6} = 10.6), which corresponds approximately to changes on the dominant electrochemical reaction pathway: CECE (pH 1–4), ECEC (pH 4–7), and EECC/EE (pH 7–14). Data were collected from 7.4 mM 2,7-AQDS solutions in 100 mM of our universal buffer and 1 M NaCl.

overpotential for 2,7-AQDS reduction, and it is consistent with the pH range at the lowest E_{drop} observed for the RFB. Conversely, the maximum ΔE_p at pH 2–4 corresponds to the maximum reaction overpotential and is consistent with the pH range at the maximum E_{drop}. Notably, the ΔE_p slightly increases at higher pH as the reaction pathway shifts towards EE. This indicates that a pH increase beyond ~10 is detrimental for the RFB VE. The transitions in the reaction pathway are also reflected in the peak current (i_p), Fig. 5d. The i_p decreases with pH in the range where CECE prevails, increases when ECEC dominates, peaking in the EECC range before decreasing again as the reaction pathway shifts to EE. The maximum peak current is obtained at pH 8–10 and coincides with the minimum ΔE_p, confirming fast reaction kinetics at this pH range. Here, we prefer to report pH ranges, instead of exact values, because pinpointing the exact minimum/maximum values would require a higher pH resolution in the experimental data.

Anolyte pH optimisation

Once the charging reaction pathway has been established, we can turn our attention to determining the optimal operational pH for the 2,7-AQDS anolyte, *i.e.* the pH of minimal overpotential. First, this is done with the aid of CV simulations and then verified *via* three-electrode cell experiments. Simulated CVs are used to avoid experimental interferences, *e.g.* electrode and membrane resistances that can mask the results. The electrochemistry simulator MECSim was used to generate the CVs.[35] The simulation method has been previously described in the literature,[36] and details on the simulation steps and parameters can be found in the SI (Table S2). CV curves simulated at pH 0–13 are shown in Fig. 6a, together with the trend in E_p (Fig. 6b), i_p (Fig. 6c) and ΔE_p (Fig. 6d). The simulated data closely match the experimental trends plotted as dashed lines in Fig. 6b–d. Simulations at smaller pH steps, Fig. 6e, can be used to pinpoint the minimum ΔE_p at pH 9.6–9.7. Thus, the minimum anolyte overpotential, and consequently the minimum E_{drop}, is expected at pH ≈ 9.6–9.7. Within the measured points, this is consistent with the experimental results obtained in the previous sections of this paper, where the minimum experimental E_{drop} and ΔE_p were observed at pH 8.6 for the full cell and at pH 9.3 for the CVs. Since ΔE_p increases for highly basic solutions (pH > 10), both experimentally and in

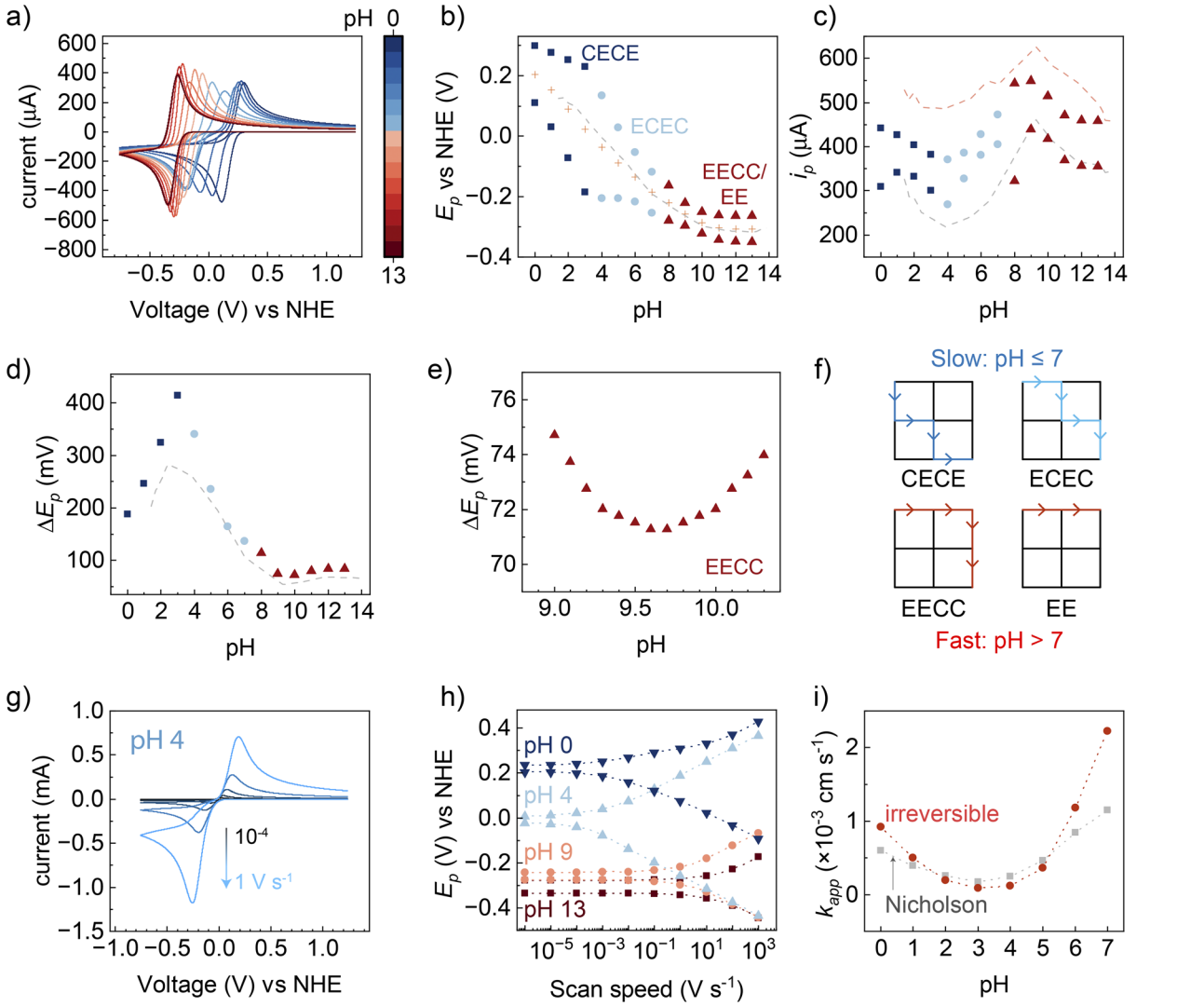

Fig. 6 Simulated kinetic data for a buffered 2,7-AQDS anolyte showing (a) CV curves, (b) peak potential (E_p), (c) peak current (i_p), (d) peak separation (ΔE_p) and (e) detail of ΔE_p at pH 9–10.3 at 100 mV s^{-1}. (f) An overview of slow and fast charging reaction pathway and pH. (g) Example of simulated CV curves at various scan speeds at pH 4, (h) Laviron curves for selected pH values, (i) apparent kinetic constant (k_{app}) extracted from Laviron curves assuming totally irreversible or quasireversible (Nicholson) systems. Simulation parameters are given in the SI (Table S2).

the simulations, it confirms that minimum voltage losses would be expected when the anolyte is buffered at mildly basic pH 8–10.

Crucially, this simulation method can be applied to estimate the minimum reduction overpotential of other quinones with known charging reaction pathways, see the SI (Fig. S7) for simulated data on anthraquinone-2-sulfonic acid (2-AQMS). As a general trend, experimental and simulation results show that charge transfer kinetics is sluggish when a CECE or ECEC reaction pathway dominates (pH ≤ 7 for the 2,7-AQDS molecule), and fast when EECC/EE prevails (pH > 7 for the 2,7-AQDS molecule), as summarised in Fig. 6f.

After modelling the optimal operational pH for 2,7-AQDS anolyte, we can investigate the slower CECE and ECEC reaction pathways. First, CVs are simulated at different scan speeds for the whole pH range 0–13 with electrode resistance set to zero. Fig. 6g shows an example for pH 4. Then, the E_p is plotted as a function of scan speed to obtain the Laviron curves, as shown for selected pH values in Fig. 6h.[44] A small ΔE_p indicates a fast reversible reaction pathway (*e.g.* curves for pH 9 and pH 13), while high ΔE_p indicates a slow irreversible reaction pathway (*e.g.* curves for pH 0 and pH 4).[39] For the slower kinetics (pH 0–7), the equation for a totally irreversible system[38,39] and the Nicholson method (quasireversible system)[40,41] were used to model an apparent kinetic constant (k_{app}), as described in the SI (apparent kinetic constant (k_{app})). The plot in Fig. 6i shows that the minimum k_{app}, *i.e.* slowest kinetic and expected worst voltage loss, is observed at pH 3 according to our model. Again, within the measured points, this is consistent with the experimental results obtained in the previous sections, where maximum experimental E_{drop} was observed at pH 3.5 for the full cell and maximum ΔE_p was observed at pH 2.4 for the CVs. This supports the overall experimental trend, with maximum voltage losses expected when the anolyte is buffered at acidic pH ≈ 2–4.

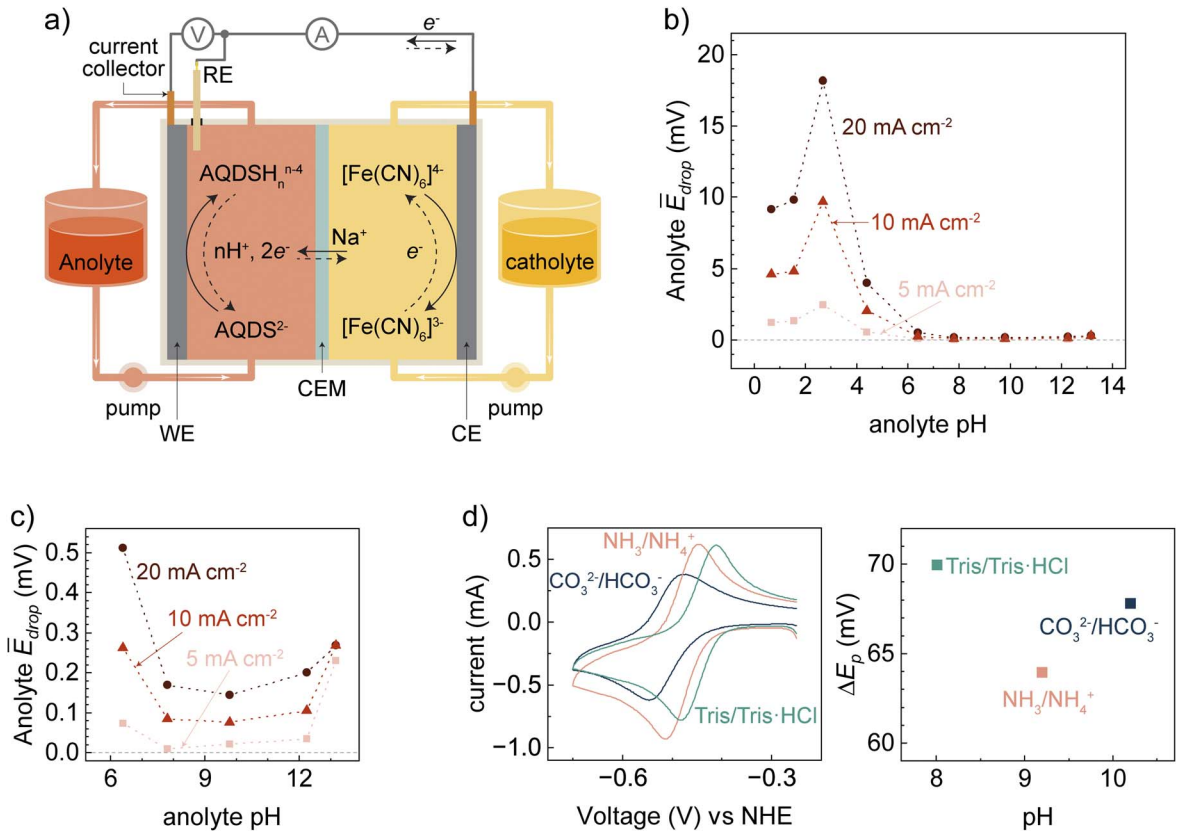

Fig. 7 (a) Schematic representation of redox flow battery cell with a three-electrode arrangement (full lines represents charging while dashed lines represent discharging), (b) measured voltage drop at the anolyte side averaged from three full charge–discharge cycles ($\bar{E}_{drop}$) and (c) detail of $\bar{E}_{drop}$ at higher pH at 5, 10 and 20 mA cm^{-2}. (d) CV curves and peak separation for 2,7-AQDS solutions buffered with 0.5 M CO_3^{2-}/HCO_3^-, 0.5 M NH_3/NH_4^+ or 0.5 M tris/tris·HCl collected at a scan rate of 100 mV s^{-1}. The data was collected from electrolytes containing ~10 mM 2,7-AQDS.

For more precise results, the E_{drop} can be directly measured at the anolyte side of the battery using a reference electrode. This excludes any possible interference from the cathode side and membrane on the results. Fig. 7a shows a scheme of the three-electrode cell used here. Here, E_{drop} is averaged over 3 full charge–discharge cycles ($\bar{E}_{drop}$). The effect of pH on the anolyte $\bar{E}_{drop}$ is clear. As expected from the simulated model, CVs and full cell results; $\bar{E}_{drop}$ is significantly higher at low pH, with a maximum at pH 2.7 ($\bar{E}_{drop}$ = 18 mV at 20 mA cm^{-2}), Fig. 7b. For pH > 6, $\bar{E}_{drop}$ decreases by approximately one order of magnitude, reaching a minimum at pH ≈ 8–10, depending on the charging rate ($\bar{E}_{drop}$ = 0.14 mV at 20 mA cm^{-2} and pH 9.8), as highlighted in Fig. 7c. Notably, within the measured points, the experimental pH values that correspond to minimum/maximum $\bar{E}_{drop}$ (9.8/2.7) closely match the pH values for simulated minimum/maximum ΔE_p (9.6/3).

In practical RFBs, pH buffering can be achieved by using common counter ions and supporting electrolytes. To illustrate this, we tested three simple buffer systems: CO_3^{2-}/HCO_3^-, NH_3/NH_4^+ and tris/tris·HCl. These buffers could be easily implemented in the anolyte tank to keep the pH at an ideal range (pH 8–10). Fig. 7d shows the CVs and ΔE_p for ~10 mM 2,7-AQDS in 0.5 M solutions of each buffer. As anticipated, the lowest peak separation is obtained for NH_3/NH_4^+, which buffers the electrolyte at pH ≈ 9.2 and should result in devices with smallest voltage losses. Notably, these results shed light on empirical observations that RFBs with close to neutral or mildly basic quinone anolytes[16,45–47] perform better than highly acidic or highly alkaline anolytes[22,48,49] of the same quinone. In particular, high performance has been reported for RFBs that use NH_4^+ as supporting electrolyte or counter ion for the 2,7-AQDS anion.[17,50] Not only does NH_4^+ act to improve 2,7-AQDS solubility, as established in previous work,[6] but the NH_4^+/NH_3 buffer system is formed during 2,7-AQDS charging. If a sufficiently high concentration of NH_4^+ is used as supporting electrolyte or counter ion, NH_4^+/NH_3 will buffer the anolyte pH close to the ideal range (pH 8–10) throughout the whole charge–discharge cycle.

Conclusions

The efficiency of an SRFB with buffered 2,7-AQDS anolyte was investigated over a broad pH range. Buffering was shown to be a viable strategy for achieving an adequate voltage match and maximising the SRFB round trip efficiency. Further investigation revealed a strong pH dependence in VE for the buffered 2,7-AQDS anolyte. At low pH values (0–7), the sluggish kinetics

attributed to the CECE and ECEC reaction pathways led to significant voltage losses during the charge–discharge cycle. In contrast, the highest VE (smallest E_{drop}) was observed at slightly alkaline anolyte pH 8–10, attributed to the predominance of the fast EECC reaction pathway. According to our numerical model, the minimum ΔE_p was calculated at pH 9.6 and 9.7, which closely matches the pH at minimum $\bar{E}_{drop}$ measured in our three-electrode experiment (pH 9.8). As a final remark, for optimal VE, it may be inferred from our results that other quinone-based RFBs may require buffering within a specific pH range. For 2,7-AQDS anolytes, this optimal range lies between pH 8 and 10, with maximum VE expected at pH 9.6–9.8.

Conflicts of interest

There are no conflicts to declare.

Data availability

The data that support the findings of this study are provided in the supplementary information (SI). The data is also available from the corresponding author upon reasonable request. Supplementary information is available. See DOI: https://doi.org/10.1039/d6ta00758a.

Acknowledgements

The authors acknowledge support for this work from Danmarks Frie Forskningsfond, research grant 0217-0033B (STORSOL).

References

1 J. Winsberg, T. Hagemann, T. Janoschka, M. D. Hager and U. S. Schubert, *Angew. Chem., Int. Ed.*, 2017, **56**, 686–711.
2 M. Pan, M. Shao and Z. Jin, *SmartMat*, 2023, **4**, e1198.
3 D. Emmel, S. Kunz, N. Blume, Y. Kwon, T. Turek, C. Minke and D. Schröder, *Nat. Commun.*, 2023, **14**, 6672.
4 G. Yang, Y. Zhu, Z. Hao, Y. Lu, Q. Zhao, K. Zhang and J. Chen, *Adv. Mater.*, 2023, **35**, 2301898.
5 F. Hasan, V. Mahanta and A. A. Abdelazeez, *Adv. Mater. Interfaces*, 2023, **10**, 2300268.
6 B. Hu, J. Luo, M. Hu, B. Yuan and T. L. Liu, *Angew. Chem., Int. Ed.*, 2019, **58**, 16629–16636.
7 M. Quan, D. Sanchez, M. F. Wasylkiw and D. K. Smith, *J. Am. Chem. Soc.*, 2007, **129**, 12847–12856.
8 L. Zhang, R. Feng, W. Wang and G. Yu, *Nat. Rev. Chem.*, 2022, **6**, 524–543.
9 K. Wedege, E. Dražević, D. Konya and A. Bentien, *Sci. Rep.*, 2016, **6**, 39101.
10 S. Jin, Y. Jing, D. G. Kwabi, Y. Ji, L. Tong, D. De Porcellinis, M. A. Goulet, D. A. Pollack, R. G. Gordon and M. J. Aziz, *ACS Energy Lett.*, 2019, **4**, 1342–1348.
11 J. Luo, B. Hu, M. Hu, Y. Zhao and T. L. Liu, *ACS Energy Lett.*, 2019, **4**, 2220–2240.
12 W. Li, H. C. Fu, L. Li, M. Cabán-Acevedo, J. H. He and S. Jin, *Angew. Chem., Int. Ed.*, 2016, **55**, 13104–13108.
13 C. Costentin, *Chem. Rev.*, 2008, **108**, 2145–2179.
14 S. H. DuVall and R. L. McCreery, *Anal. Chem.*, 1999, **71**, 4594–4602.
15 Q. Lin, Q. Li, C. Batchelor-Mcauley and R. G. Compton, *J. Phys. Chem. C*, 2015, **119**, 1489–1495.
16 F. Fenini, E. Drazevic and A. Bentien, *J. Power Sources*, 2022, **540**, 231641.
17 A. Khataee, K. Wedege, E. Dražević and A. Bentien, *J. Mater. Chem. A Mater.*, 2017, **5**, 21875–21882.
18 S. Srinivas, K. Ashokkumar, K. Sriraghavan and A. Senthil Kumar, *Sci. Rep.*, 2021, **11**, 13905.
19 R. J. Forster and J. P. O'Kelly, *J. Electroanal. Chem.*, 2001, **498**, 127.
20 W. D. McCulloch, M. Yu and Y. Wu, *ACS Energy Lett.*, 2016, **1**, 578–582.
21 K. Wedege, D. Bae, W. A. Smith, A. Mendes and A. Bentien, *J. Phys. Chem. C*, 2018, **122**, 25729–25740.
22 K. Wedege, J. Azevedo, A. Khataee, A. Bentien and A. Mendes, *Angew. Chem., Int. Ed.*, 2016, **55**, 7142–7147.
23 W. Li, J. Zheng, B. Hu, H. C. Fu, M. Hu, A. Veyssal, Y. Zhao, J. H. He, T. L. Liu, A. Ho-Baillie and S. Jin, *Nat. Mater.*, 2020, **19**, 1326–1331.
24 W. Li, H. C. Fu, Y. Zhao, J. H. He and S. Jin, *Chem*, 2018, **4**, 2644–2657.
25 K. Wedege, D. Bae, E. Dražević, A. Mendes, P. C. K. Vesborg and A. Bentien, *RSC Adv.*, 2018, **8**, 6331.
26 T. Tichter, K. Naumann and P. C. K. Vesborg, *Electrochim. Acta*, 2024, **487**, 144140.
27 W. Li and S. Jin, *Acc. Chem. Res.*, 2020, **53**, 2611–2621.
28 W. Li, E. Kerr, M. A. Goulet, H. C. Fu, Y. Zhao, Y. Yang, A. Veyssal, J. H. He, R. G. Gordon, M. J. Aziz and S. Jin, *Adv. Energy Mater.*, 2019, **9**, 1900918.
29 D. A. Ellis, *Nature*, 1961, **191**, 1099–1100.
30 H. T. S. Britton and R. A. Robinson, *J. Chem. Soc.*, 1931, 458–473.
31 T. J. Carney, S. J. Collins, J. S. Moore and F. R. Brushett, *Chem. Mater.*, 2017, **29**, 4801–4810.
32 R. Nielsen, T. H. Youngman, A. Crovetto, O. Hansen, I. Chorkendorff and P. C. K. Vesborg, *ACS Appl. Energy Mater.*, 2021, **4**, 10697–10702.
33 T. H. Youngman, R. Nielsen, A. Crovetto, B. Seger, O. Hansen, I. Chorkendorff and P. C. K. Vesborg, *Sol. RRL*, 2021, **5**, 2100111.
34 R. Nielsen, T. H. Youngman, H. Moustafa, S. Levcenco, H. Hempel, A. Crovetto, T. Olsen, O. Hansen, I. Chorkendorff, T. Unold and P. C. K. Vesborg, *J. Mater. Chem. A Mater.*, 2022, **10**, 24199.
35 G. F. Kennedy, A. M. Bond and A. N. Simonov, *Curr. Opin. Electrochem.*, 2017, **1**, 140–147.
36 C. Batchelor-McAuley, Q. Li, S. M. Dapin and R. G. Compton, *J. Phys. Chem. B*, 2010, **114**, 4094–4100.
37 C. Wiberg, T. J. Carney, F. Brushett, E. Ahlberg and E. Wang, *Electrochim. Acta*, 2019, **317**, 478–485.
38 C. V. S. Biologic, *Simulation of the Simple Redox Reaction (E) – Part I: the Effect of Scan Rate Kinetics – Application Note 41-1*, 2022.
39 A. J. Bard and L. R. Faulkner, *Electrochemical Methods Fundamentals and Applications*, 2nd edn, 2001, vol. 48.

40 R. S. Nicholson, *Anal. Chem.*, 1965, **37**, 1351–1355.
41 I. Lavagnini, R. Antiochia and F. Magno, *Electroanalysis*, 2004, **16**, 505–506.
42 R. Nielsen, A. Crovetto, A. Assar, O. Hansen, I. Chorkendorff and P. C. K. Vesborg, *PRX Energy*, 2024, **3**, 013013.
43 J. B. Conant, H. M. Kahn, L. F. Fieser and S. S. Kurtz, *J. Am. Chem. Soc.*, 1922, **44**, 1382–1396.
44 E. Laviron, *J. Electroanal. Chem.*, 1979, **101**, 19–28.
45 W. Lee, A. Permatasari and Y. Kwon, *J. Mater. Chem. C Mater.*, 2020, **8**, 5727–5731.
46 G. Yang, Y. Zhu, Z. Hao, Q. Zhang, Y. Lu, Z. Yan and J. Chen, *Adv. Energy Mater.*, 2024, **14**, 2400022.
47 Y. Ji, M. A. Goulet, D. A. Pollack, D. G. Kwabi, S. Jin, D. De Porcellinis, E. F. Kerr, R. G. Gordon and M. J. Aziz, *Adv. Energy Mater.*, 2019, **9**, 1900039.
48 E. M. Fell and M. J. Aziz, *J. Electrochem. Soc.*, 2023, **170**, 100507.
49 D. G. Kwabi, K. Lin, Y. Ji, E. F. Kerr, M. A. Goulet, D. De Porcellinis, D. P. Tabor, D. A. Pollack, A. Aspuru-Guzik, R. G. Gordon and M. J. Aziz, *Joule*, 2018, **2**, 1894–1906.
50 G. Tian, R. Jervis and A. J. Sobrido, *Electrochim. Acta*, 2023, **461**, 142671.